Evidence of Wolframite-Type Structure in Ultrasmall Nanocrystals with a Targeted Composition MnWO 4

Pascaline Patureau, Remi Dessapt, Pierre-Emmanuel Petit, Gautier Landrot, Christophe Payen, Philippe Deniard

Evidence of wolframite-type structure in ultrasmall nanocrystals with a targeted composition $MnWO_4$

Pascaline Patureau[1], Rémi Dessapt[1], Pierre-Emmanuel Petit[1], Gautier Landrot[2], Christophe Payen[1,*], Philippe Deniard[1,*]

[1] Institut des Matériaux Jean Rouxel (IMN), Université de Nantes, CNRS, 2 rue de la Houssinière, BP 32229, 44322 Nantes cedex 3, France

[2] Synchrotron SOLEIL, F-91192 Gif sur Yvette, France

*Authors to whom inquiries regarding the paper may be addressed

ABSTRACT: Here, we report a study of white-ochre powders with targeted composition $MnWO_4$ prepared via a coprecipitation method. Through X-ray total scattering combined with pair distribution function analysis and Rietveld refinement of X-ray diffraction data we find that their crystal structure is similar to that of bulk-$MnWO_4$, despite a mean crystallite size of 1.0-1.6 nm and a significant deviation of the average chemical composition from $MnWO_4$. The chemical formula derived from elemental and thermogravimetric analyses is $Mn_{0.8}WO_{3.6}(OH)_{0.4}.3H_2O$. X-ray absorption and magnetic susceptibility measurements show that Mn and W have the same oxidation states as in $MnWO_4$. No magnetic ordering or spin glass or superparamagnetic behavior is observed above 2 K, unlike in the case of $MnWO_4$ nanocrystals having mean size higher than 10 nm.

■ INTRODUCTION

Transition metal tungstates of the MWO_4 type (M = Mn, Fe, Co, Ni, Cu, or Zn) have attracted great interest due to potential applications in various fields, including humidity sensors[1], multiferroic materials[2], photocatalysts[3], heterogeneous catalysts[4], biomedical imaging[5], energy storage materials[6], and color pigments[7]. These compounds contain M(II) and tungsten(VI) cations in octahedral environments. They crystallize with the wolframite (monoclinic) structure[8], with the exception of $CuWO_4$ which exhibits a lower (triclinic) crystal symmetry associated with cooperative Jahn-Teller distortions of the Cu^{2+} (d^9) environment[9]. Crystal structures comprise infinite zigzag $(MnO_4)_\infty$ and $(WO_4)_\infty$ chains, running parallel to the same direction, of either edge-sharing MO_6 distorted octahedra or edge-sharing WO_6 distorted octahedra.[8-10] Their interesting properties have been investigated at different length scales, from bulk in single crystals or fine particles to nanoscale in nanosized materials. For applications or studies at the nanoscale, a possible key challenge is keeping crystal structures with high crystallinity and their associated bulk properties when decreasing particle size. For $MnWO_4$, which is a well-studied multipurpose material[1,2,5,6], phase-pure nanoparticles of controlled size and shape have been prepared by mild solution methods[11,12], and single-crystal nanoparticles with mean size in the range of 10-50 nm have been studied[13-15]. When looking at their structure-dependent bulk electronic properties, one can note that magnetic transitions associated with type-II multiferroicity in bulk-$MnWO_4$ are still visible in temperature-dependent magnetic susceptibility curves of ≈ 50 nm *single-crystal* nanopellets and nanorods[15] but are absent when mean crystallite size is ≈ 10 nm[14].

Here, we address the problem of how the wolframite structural order of $MnWO_4$ evolves when downscaling towards the ultrasmall nanocrystallite range (≤ 5-10 nm) where unique physicochemical properties are generally observed[16]. This unresolved issue also deserved attention with regards to the chemistry of transition metal tungstate nanoparticle

formation.[17] In this work, we have studied the crystal structure and metal oxidation states in ultrasmall nanocrystals with targeted composition $MnWO_4$ through X-ray total scattering combined with pair distribution function analysis (PDF), X-ray diffraction (XRD), X-ray Absorption Near Edge Structure (XANES) spectroscopy, and magnetic susceptibility measurements. Samples were prepared by using a coprecipitation method that produces a white-ochre solid. Although the formation of a white-ochre precipitate with unknown chemical formula has already been observed in a few previous works[18,19] which employed a co-precipitation method, no characterization data has been reported so far. We therefore have also determined the actual macroscopic chemical formula and have examined the thermal stability of these precipitates in air by variable temperature XRD.

■ EXPERIMENTAL SECTION

Synthesis, Elemental and Thermogravimetric Analyses. High-purity reagent chemicals were purchased from commercial vendors. Elemental analyses (Mn, W, Na, and H contents) were performed on as-prepared powders at the "Service Central d'Analyse du CNRS", Vernaison, France. Thermogravimetric measurements were performed in flowing air. Powders were placed in alumina crucibles and heated up to 800°C at 3 K /min.

Characterization. Attempts at carrying out transmission electron microscopy experiments failed because samples were unstable. X-ray diffraction (XRD) patterns were collected at room temperature on a Bruker D8 Advance instrument using monochromatic $Cu_{K\text{-}L3}$ (λ = 1.540598 Å) X-rays and a LynxEye detector. Temperature variable XRD experiments were carried out on a Bruker D8 Advance instrument using $Cu_{KL2\text{-}L3}$ (λ = 1.540598, 1.54433 Å) radiation and a Våntec detector. Le Bail and Rietveld analyses of the XRD data were

performed using JANA 2006[20] and the Cheary-Coelho fundamental approach for XRD profile parameters[21].

X-ray Absorption Spectroscopy analyses were done at SAMBA beamline, Synchrotron SOLEIL. The storage ring was operated with multi-bunch and top-up modes, with 2.75 GeV electron energy and 450 mA current. Powder samples were pelletized prior acquisition and analyzed at room temperature. X-ray Absorption Near Edge Structure (XANES) spectra were collected at the W L_3 edge (10207 eV) and Mn K edge (6539 eV) in fluorescence mode using a Si(220) monochromator, a Ge multi-pixel fluorescence detector (Canberra), and step-by-step acquisition mode. At each edge, multiple spectra were collected until the signal-to-noise ratio of the corresponding merge spectrum was satisfactory. All spectra were averaged, normalized and corrected from self-absorption effects using Athena featured in Demeter Software Package.[22]

X-ray total scattering measurements were performed at room temperature on a Bruker D8 Advance instrument using $Mo_{KL2\text{-}L3}$ (λ = 0.70929, 0.71358 Å) radiation and a Våntec detector. This set up produces, for a 2θ range up to 150°, a Q_{max} of 17 $Å^{-1}$. Observed PDFs were calculated using PDFgetX2 software[23] and real space refinements were performed using PDFgui[24].

A Quantum Design MPMS-XL7 magnetometer was used to collect temperature-dependent DC magnetization data. Zero field cooled (ZFC) and field cooled (FC) magnetization measurements were taken from 2 to 300 K in an applied field of $\mu_0 H$ = 0.01 or 0.1 T. Data were corrected for the diamagnetism of the sample holder as well as for core diamagnetism using Pascal's constants[25].

■ RESULTS AND DISCUSSION

Synthesis and Compositional Analysis. Samples with a targeted Mn:W molar ratio of 1.0 were prepared in a reproducible manner by using a coprecipitation method.[26] Aqueous solution of manganese chloride $MnCl_2.4H_2O$ (0.6 mmol in 10 mL) was added slowly to an aqueous solution of $Na_2WO_4.2H_2O$ (0.6 mmol in 10 mL) at room temperature under vigorous magnetic stirring, leading to immediate precipitation of a white-ochre solid. The pH was kept constant at about 7 by adding manually HCl 0.1 M and the slurry was stirred at room temperature for five minutes. After filtration, the powder was washed with water, ethanol, and dried in air at room temperature. The final yield in W was 22 mol%. Elemental analyses showed no evidence for incorporation of sodium cations and were in good agreement with the chemical composition $H_{6.4}Mn_{0.8}WO_{7.0}$ that fulfills electroneutrality (see the Supporting Information). Thermogravimetric data are shown in Figure 1. A total mass loss of about 19 % took place in three steps in the temperature range of 25-800 °C. The small mass loss of ≈ 1.5 % observed below ≈ 50 °C is likely due to the removal of free and/or physisorbed water. Thermogravimetric data also revealed a mass loss of ≈ 15.5 % in the temperature range of 50-150° C and ≈ 2% in the temperature range of 150-800 °C. By rewriting the chemical formula $H_{6.4}Mn_{0.8}WO_{7.0}$ as $Mn_{0.8}WO_{3.6}(OH)_x.yH_2O$, mass loss calculations indicated that the weight losses of 15.5 % and 2% correspond to the losses of 3 H_2O and 0.4 (OH), respectively. Therefore, the chemical formula was considered to be $Mn_{0.8}WO_{3.6}(OH)_{0.4}.3H_2O$. Quantitative analysis of the XRD pattern at 700°C and magnetic susceptibility data were also fully consistent with this formula as described hereafter. The low Mn:W ratio in the precipitate (0.8) agrees with the results in ref. 26 and implies the presence of unreacted Mn(II) cations in solution. These Mn(II) cations actually react with $Mn_{0.8}WO_{3.6}(OH)_{0.4}.3H_2O$ to yield $MnWO_4$ nanopellets when the white-ochre slurry is hydrothermally treated at 180°C[15].

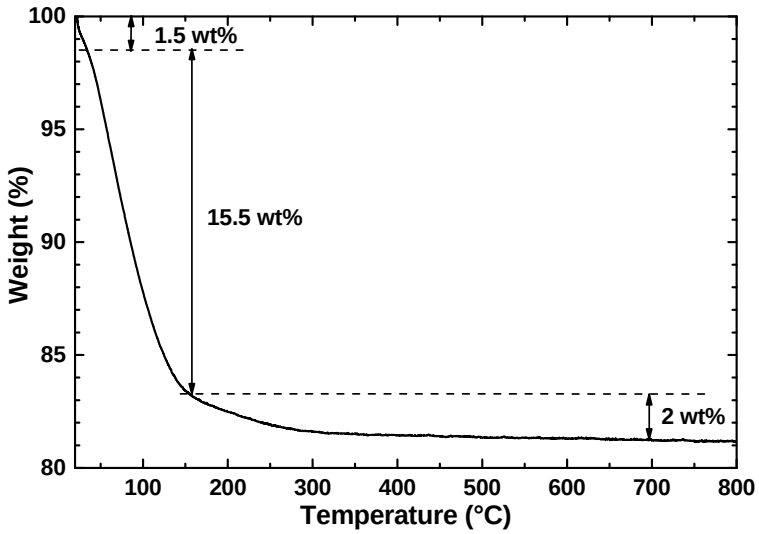

Figure 1. Thermogravimetric curve for $Mn_{0.8}WO_{3.6}(OH)_{0.4}.3H_2O$ in flowing air.

Variable Temperature X-ray Diffraction. Figure 2 (25° C) presents the room temperature XRD pattern of as-prepared powder. No distinct Bragg reflections was observed and thus the compound could at first sight be considered to be amorphous. Three very broad features centered at $2\theta \approx 30$, 55, and 65° were however visible in the XRD pattern and the absence of narrow Bragg reflections could instead be due to strong peak broadening and overlap. Syntheses of powder samples of $MnWO_4$ via co-precipitation are usually followed by a brief heating in air at a moderate temperature, e.g., 400-500 °C, that makes it possible to observe narrow Bragg reflections in XRD patterns[26]. Figure 2 also shows the evolution of the diffraction pattern as a function of temperature. At 450 °C, the diffraction pattern was similar to that of $MnWO_4$ (ICSD # 67907). Above 450 °C small additional peaks appeared. They were observed up to 700 °C as evidenced by the inset of Figure 2 where they are marked with asterisks. They correspond to the krasnogorite variety of WO_3 (pdf file 71-0131). A two-phase refinement carried out by the Rietveld method for 700°C (see Figure S1 in the Supporting Information), leaded to 14.8 +/- 1.2 wt% of WO_3 in perfect agreement with complete thermal decomposition of $Mn_{0.8}WO_{3.6}(OH)_{0.4}.3H_2O$ into $MnWO_4$ plus WO_3, in air.

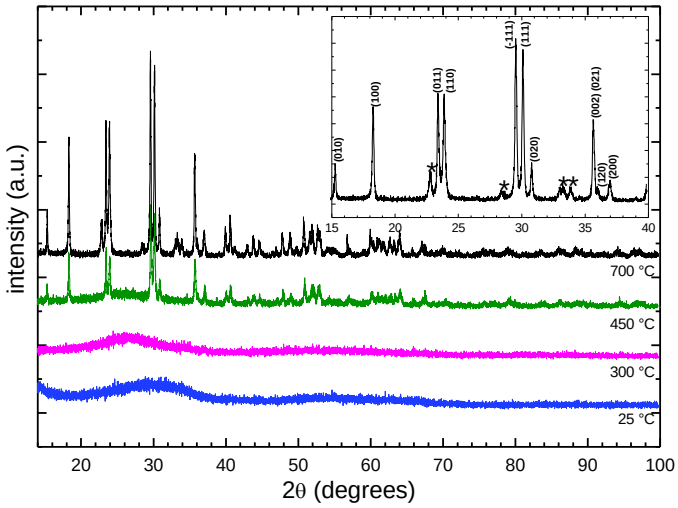

Figure 2. X-ray diffraction patterns of $Mn_{0.8}WO_{3.6}(OH)_{0.4}.3H_2O$ taken with CuK_{L2-L3} radiation. Patterns were collected in air at several temperatures from 25 to 700 °C (temperature is indicated below the corresponding pattern) using the same powder for the whole data set. The inset shows a portion of the pattern recorded at 700°C. Bragg reflections marked with asterisks are from WO_3. *hkl* indices are those of $MnWO_4$ (ICSD 67907).

X-ray Absorption Near Edge Structure (XANES). XANES was used in order to determine oxidation states and local environments of Mn and W in $Mn_{0.8}WO_{3.6}(OH)_{0.4}.3H_2O$. Figure 3 presents W L_3 and Mn *K* edge spectra for both the $Mn_{0.8}WO_{3.6}(OH)_{0.4}.3H_2O$ precipitate and a well characterized micrometric powder of $MnWO_4$. This figure also shows our W L_3 XANES data for the reactant $Na_2WO_4.2H_2O$, which contains W(VI) ions in tetrahedral environment.[27] For each edge, spectra were collected under the same experimental conditions. The ionic state and local environment of W can be identified by comparing the onset energies and shapes of the W L_3 spectra.[28] From data in Figure 3, it is evident that tungsten is exclusively found in the form of W(VI) in octahedral environment, just like in $MnWO_4$. For the Mn *K* edge data,

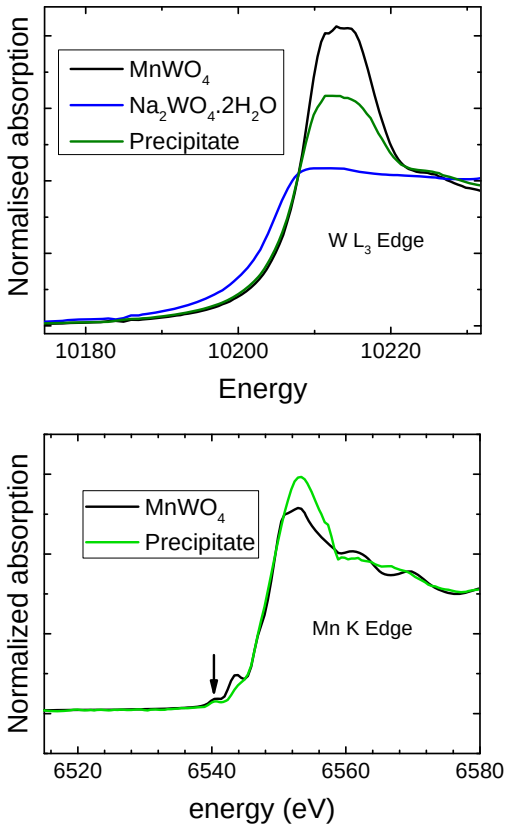

Figure 3. XANES spectra for $Mn_{0.8}WO_{3.6}(OH)_{0.4}.3H_2O$ (termed Precipitate) and for micrometric powder of $MnWO_4$. Top panel: W L_3-edge spectra. Data for $Na_2WO_4.2H_2O$ were also recorded for the sake of comparison. Bottom panel: Mn *K* edge spectra. The arrow indicates pre-edge features at ≈ 6540 eV which are related to electronic transitions to *1s* core levels to empty hybridized *3d/4p* states.

---

determination of the Mn oxidation state from the main edge energy is not possible due to single and multiple scattering effects.[29] However, the weak pre-edge features observed at about 6540 eV for both $Mn_{0.8}WO_{3.6}(OH)_{0.4}.3H_2O$ and $MnWO_4$ clearly indicate the presence of Mn(II) in octahedral symmetry.[29]

Pair Distribution Function (PDF) Analysis. A PDF analysis of X-ray total scattering data was then performed to study the interatomic distances *r*. Total scattering structure factors *S(Q)* of both $Mn_{0.8}WO_{3.6}(OH)_{0.4}.3H_2O$ and micrometric $MnWO_4$ are presented in Figure S2 in the Supporting Information to visualize the quality of the data treatment. Figure 4 shows the PDF, *G(r)*, of $Mn_{0.8}WO_{3.6}(OH)_{0.4}.3H_2O$. Peaks in the low *r*-region of the PDF were compared

to those observed in the PDF of a micrometric powder sample of $MnWO_4$, which is also shown in Figure 4. The calculated PDF of the published wolframite structure of bulk $MnWO_4$ (ICSD # 67907)[10] is presented in Figure 5 for the sake of comparison. For $Mn_{0.8}WO_{3.6}(OH)_{0.4}.3H_2O$, the two peaks at about 1.8 and 2.3 Å correspond well to the mean metal-oxygen distances in WO_6 and MnO_6 octahedra of the bulk-$MnWO_4$ structure, respectively. As in bulk-$MnWO_4$, a weak peak at ≈ 2.9 Å can be associated with oxygen-oxygen distances. The large and intense peak at 3.6 Å is likely due to the shortest metal-metal distances; Mn-Mn or W-W distances for edge-sharing MnO_6 or WO_6 octahedra that form the $(MnO_4)_n$ or $(WO_4)_n$ chains, and Mn-W distances for two MnO_6 and WO_6 octahedra sharing a corner. Furthermore, the two peaks found between 4 and 5 Å match with the W-W distances of 4.45 and 4.8 Å in bulk-$MnWO_4$. All these observations prompted us to perform a refinement of the PDF of $Mn_{0.8}WO_{3.6}(OH)_{0.4}.3H_2O$ using the bulk-$MnWO_4$ crystallographic model with a size damping envelope. The obtained fit, shown in Figure 4, was of good quality up to about 6 Å.

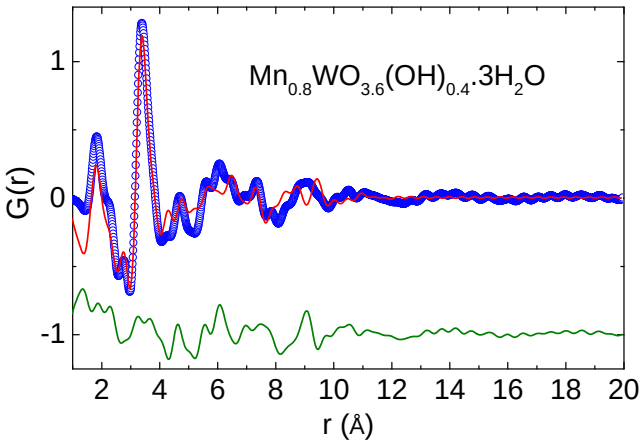

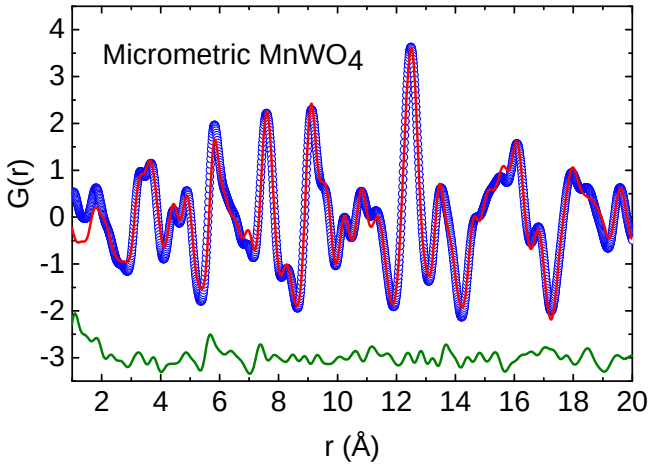

Figure 4. Experimental PDF *G(r)* for $Mn_{0.8}WO_{3.6}(OH)_{0.4}.3H_2O$ (top panel) and for a micrometric powder sample of $MnWO_4$ (bottom panel) derived from X-ray total scattering data taken with Mo Kα1 Kα2 radiations (blue dots). The red lines show fits obtained using (i) a $MnWO_4$ particle model in the case of $Mn_{0.8}WO_{3.6}(OH)_{0.4}.3H_2O$ (ii) the published wolframite structure model of bulk-$MnWO_4$ in the case of micrometric $MnWO_4$. The lower green curves show the differences between the PDF and the refinement.

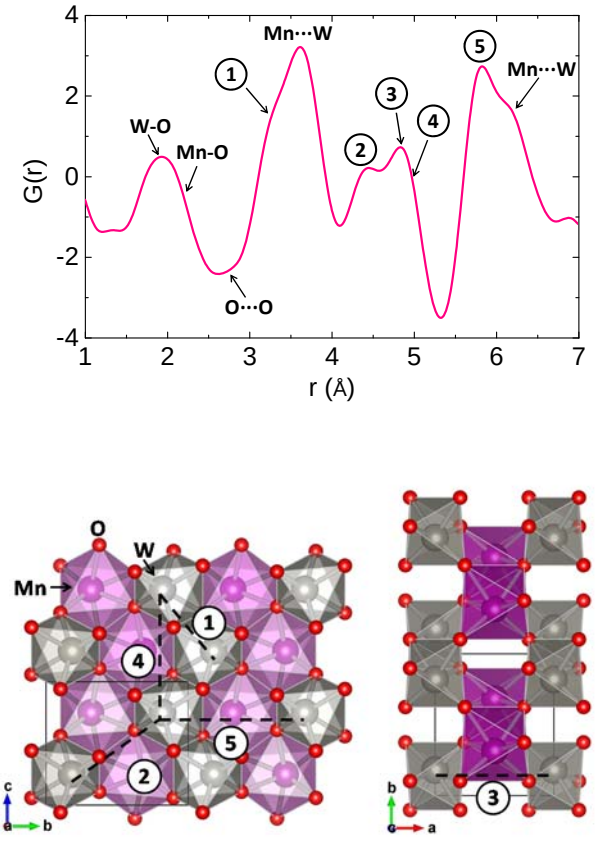

Figure 5. Calculated PDF *G(r)* of the published wolframite bulk-$MnWO_4$ model in the low *r*-region. Some interatomic distances are shown above or below the PDF. The five shortest W-W distances are marked with numbers (1 to 5) and are illustrated on the perspective views of the crystal structure shown below the graph.

Difficulty in refining the PDF for longer distances correlates with the ultrasmall fitted particle size, 1.3 ± 0.3 nm. A spherical nanocrystal of $MnWO_4$ with a diameter of 1.3 nm would consist of about 8 unit cells and ≈ 100 atoms, a significant number of which would be located on the surface. Deviation from the bulk $MnWO_4$ composition, which includes a lower Mn-to-W ratio of 0.8 and the incorporation of hydroxides into particle structure, could also explain differences in local structure.

Rietveld refinement and simulation of room-temperature XRD data. According to our PDF analysis, the room-temperature XRD pattern of $Mn_{0.8}WO_{3.6}(OH)_{0.4}.3H_2O$ should be consistent with ultrasmall ≈ 1 nm nanocrystallites having a $MnWO_4$-type structure. Thus, we performed a Rietveld refinement using the published bulk-$MnWO_4$ structural model.[10] Given the low signal-to-noise ratio and the large width of Bragg reflections, only the following parameters were refined: scale factor, crystallite size and background (5-term Legendre polynomial). All $MnWO_4$ structural parameters (taken from ICSD # 67907) were held fixed. The refinement converged to obtain the results shown in Figure 6, which were in very good agreement with a nanoscale $MnWO_4$-like compound. The refined crystallite size 0.82(2) nm compares well with the value 1.3(3) nm derived from PDF analysis, given that microstrains could not be taken into account in the contribution to line broadening. An additional clue about the nanocrystalline nature of $Mn_{0.8}WO_{3.6}(OH)_{0.4}.3H_2O$ is provided by Figure S3 (Supporting Information). In this latter figure, the X-ray diffraction pattern of $MnWO_4$ (ICSD # 67907) was simulated for two different crystallite sizes (50 and 1 nm) and for $Cu_{K\text{-}L3}$ radiation. In the 1 nm case, the simulated pattern, which is very similar to that shown in

Figure 6, results solely from overlap of many Bragg reflections and does not correspond to that of an amorphous material.

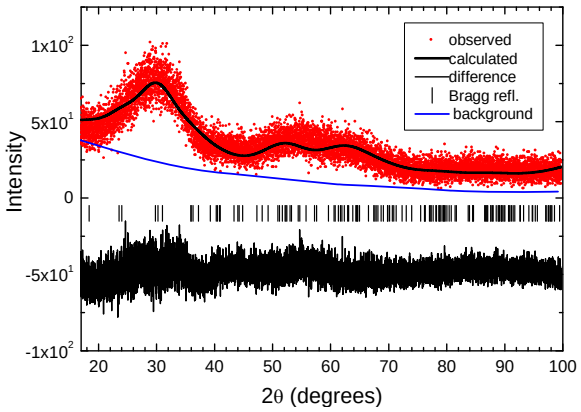

Figure 6. Final Rietveld refinement plot of the room-temperature XRD data (taken with $Cu_{K\text{-}L3}$ radiation) for $Mn_{0.8}WO_{3.6}(OH)_{0.4}.3H_2O$. This refinement was performed using the published bulk-$MnWO_4$ structural model. The blue line shows the fitted background. Each *hkl* reflection, as represented by a vertical bar, overlaps with its neighbors, leading to a few broad features in the pattern.

Magnetic susceptibility. Finally, we turn to the magnetic properties. Temperature dependent magnetic susceptibility data, $\chi(T)$, of as-prepared powders were collected from 2 to 300 K. As can be seen in Figure 7, the magnetic susceptibility obeys a Curie-Weiss law above ≈ 25 K. The molar Curie constant calculated using the molar mass of $Mn_{0.8}WO_{3.6}(OH)_{0.4}.3H_2O$ is actually the one expected for 0.8 mole of Mn(II) ions having $S = 5/2$ spin and for nonmagnetic W(VI) ions. Data in Figure 8 also indicate the absence of magnetic orders or superparamagnetic or spin-glass behaviors as the susceptibility keeps rising down to the base temperature (with no difference between the data measured under zero-field-cooled and that measured under field-cooled conditions). In bulk-$MnWO_4$, three magnetic structures have been observed below T_N = 13.5 K, T_2 = 12.5 K and T_1 ≈ 8 K.[30] The two transitions at T_N and

T_2 and the associated ferroelectric transition were still observed in nanocrystals with mean diameter of 50 nm[15], but only one magnetic transition was visible at 6 K in nanocrystals with mean size of 10 nm.[14] In the multiferroic state of bulk-$MnWO_4$ below T_2, the incommensurate magnetic structure has a large magnetic unit cell volume of 2.8 nm^3, which reflects the existence of long-ranged magnetic interactions.[30,31] Therefore a loss of spin-driven multiferroicity is expected in any $MnWO_4$ nanocrystallite having a volume lower than or comparable with the bulk magnetic cell volume. Deviation from $MnWO_4$ composition should also affect the magnetic properties of $Mn_{0.8}WO_{3.6}(OH)_{0.4}.3H_2O$.

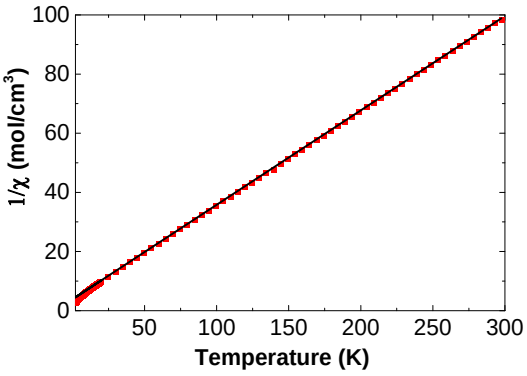

Figure 7. Inverse molar magnetic susceptibility $1/\chi$ versus temperature T for $Mn_{0.8}WO_{3.6}(OH)_{0.4}.3H_2O$. The solid line corresponds to a Curie-Weiss behavior, $1/\chi = (T-\theta)/C$, with C = 3.1 cm^3 K mol^{-1} and θ = -11 K obtained from a fit to the data in the temperature range of 25-200 K.

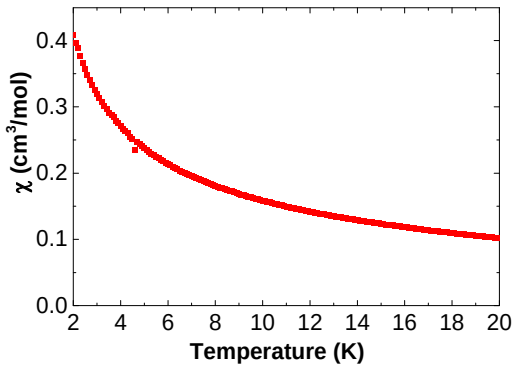

Figure 8. Magnetic susceptibility $\chi(T)$ in the low-T region, T ≤ 20 K, for $Mn_{0.8}WO_{3.6}(OH)_{0.4}.3H_2O$

■ CONCLUDING REMARKS

To summarize, white-ochre powder samples of $Mn_{0.8}WO_{3.6}(OH)_{0.4}.3H_2O$ were reproducibly obtained by a simple salt metathesis reaction involving stoichiometric amounts of manganese(II) chloride and sodium tungstate dihydrate. A common belief is that this co-precipitation method gives dispersions containing amorphous particles which would act as precursors for the hydrothermal synthesis of crystallized nanoparticles of transition metal tungstates.[13] However our study indicates that coprecipitation can lead to the formation of ultrasmall nanocrystals which retain important structural features of the bulk when synthesis conditions are chosen so as to prevent the formation of polyoxometalates in solution. In this case, there are similarities in the crystal structures between the precursor and the final nanosized $MnWO_4$ material.

■ AUTHOR INFORMATION

Corresponding authors

*Email: philippe.deniard@cnrs-imn.fr

*Email: christophe.payen@cnrs-imn.fr

Notes

The authors declare no competing financial interest.

■ ACKNOWLEDGMENTS

The authors are grateful for the beamtime obtained at beamline SAMBA at the SOLEIL synchrotron radiation source, France (project 20141046). We thank Eric Gautron and Nicolas Stephant for their attempts at performing electron microscopy.

■ REFERENCES

(1) Qu, W.; Wlodarski, W.; Meyer, J.U. Comparative study on micromorphology and humidity sensitive properties of thin-film and thickfilm humidity sensors based on semiconducting MnWO4. *Sens. Actuators B* **2000**, *64*, 76–82.
(2) Arkenbout, A. H.; Palstra, T. T. M.; Siegrist, T.; Kimura, T. Ferroelectricity in the Cycloidal Spiral Magnetic Phase of MnWO4. *Phys. Rev. B* **2006**, *74*, 184431.
(3) Montini, T.; Gombac, V.; Hameed, A.; Felisari, L.; Adami, G.; Fornasiero, P. Synthesis, characterization and photocatalytic performance of transition metal tungstates. *Chem. Phys. Lett* **2010**, *498*, 113-119.
(4) Jibril, B. Y. Catalytic Performances and Correlations with Metal Oxide Band Gaps of Metal-Tungsten Mixed Oxide Catalysts in Propane Oxydehydrogenation. *React. Kinet. Catal. Lett.* **2005**, *86*, 171-177.
(5) Zou, Q.; Tang, R.; Zhao, H.; Jiang, J.; Li, J.; Fu, Y. Hyaluronic-Acid-Assisted Facile Synthesis of MnWO4 Single-Nanoparticle for Efficient Trimodal Imaging and Liver–Renal Structure Display *ACS Appl. Nano Mater.* **2018**, *1*, 101–110.
(6) Zhang, E.; Xing, Z.; Wang, J.; Ju, Z.; Qian, Y. Enhanced energy storage and rate performance induced by dense nanocavities inside MnWO4 nanobars. *RSC Advances* **2012**, *2*, 6748–6751.
(7) Dey, S.; Ricciardo, R.A.; Cuthbert, H.L.; Woodward, P.M. Metal-to-Metal Charge Transfer in AWO4 (A = Mg, Mn, Co, Ni, Cu, or Zn) Compounds with the Wolframite Structure. *Inorg. Chem.* **2014**, *53*, 4394–4399.
(8) Sleight, A.W. Accurate Cell Dimensions for ABO4 Molybdates and Tungstates. *Acta Cryst.B* **1972**, *28*, 2899–2902.
(9) Kihlborg, L.; Gebert, E. CuWO4, a Distorted Wolframite-Type Structure. *Acta Cryst.B* **1970**, *26*, 1020-1026.
(10) Macavei, J.; Schulz, H. The crystal structure of wolframite type tungstates at high pressure. *Z.Kristallogr.* **1993**, *207*, 193-208.
(11) Chen, S.-J.; Chen, X.-T.; Xue, Z.; Zhou, J.-H.; Li, J.; Hong, J-M.; You, X.-H. Morphology control of MnWO4 nanocrystals by solvothermal route. *J. Mater. Chem.* **2003**, *13*, 1132-1135.
(12) Tong, W.; Li, L..; Hu, W.; Yan, T.; Guan, X.; Li, G. Kinetic control of MnWO4 Nanoparticles for Tailored Structural Properties. *J. Phys. Chem. C* **2010**, *114*, 15298-15305.
(13) Yu, S.-H.; Liu, B.; Mo, M.-S.; Huang, J.-H.; Liu, X.-M., and Qian, Y.-T. General Synthesis of Single-Crystal Tungstate Nanorods/Nanowires: A Facile, Low-Temperature Solution Approach. *Adv. Funct. Mater.* **2003**, *13*, 639-647.
(14) Ungelenk, J.; Roming, S.; Adler, P.; Schnelle, W.; Winterlik, J.; Felser, C.; Feldmann, C. Ultrafine MnWO4 nanoparticles and their magnetic properties. *Solid State Sciences* **2015**, *46*, 89-94.
(15) Patureau, P.; Dessapt, R.; Deniard, P.; Chung, U.-C.; Michau, D.; Josse, M.; Payen, C.; Maglione, M. Persistent Type-II Multiferroicity in Nanostructured MnWO4 Ceramics. *Chem. Mater.* **2016**, *28*, 7582-7585.
(16) Kim, B.H.; Hackett, M.J.; Park, J.; Hyeon, T. Synthesis, Characterization, and Application of Ultrasmall Nanoparticles. *Chem. Mater.* **2014**, *26*, 59-71.
(17) Bojesen, E.D.; Iversen, B.B. The chemistry of nucleation. *CrystEngComm* **2016**, *18*, 8332-8353.
(18) Thongtem, S.; Wannapop, S.; Phuruangrat, A.; Thongtem, T. Cyclic microwave-assisted spray synthesis of nanostructured MnWO4. *Materials Letters* **2009**, *63*, 833-836.
(19) Zhou, S.; Huang, J.; Zhang, T.; Ouyang H.; Li, A.; Zhang, Z. Effect of variation Mn/W molar ratios on phase composition, morphology and optical properties of MnWO4. *Ceramics International* **2013**, *39*, 5159-5163.

(20) Petricek, V.; Dusek, M.; Palatinus, L. Crystallographic Computing System JANA2006: General Features. *Z. Für Krist.* **2014**, *229*, 345–352.
(21) Cheary, R. W.; Coelho, A.A. Axial Divergence in a Conventional X-ray Powder Diffractometer. I. Theoretical Foundations. *J. Appl. Crystallogr.* **1998**, *31*, 851–861.
(22) Ravel, B.; Newville, M., ATHENA, ARTEMIS, HEPHAESTUS: data analysis for X-ray absorption spectroscopy using IFEFFIT. *Journal of Synchrotron Radiation* **2005**, *12*, 537-541.
(23) Qiu, X.; Thompson, J. W.; Billinge, S. J. PDFgetX2: a GUI-driven program to obtain the pair distribution function from X-ray powder diffraction data. *J. Appl. Crystallogr.* **2004**, *37*, 678–678.
(24) Farrow, C. L.; Juhas, P.; Liu, J. W.; Bryndin, D.; Božin, E. S.; Bloch, J.; Proffen, T.; Billinge, S. J. L. PDFfit2 and PDFgui: computer programs for studying nanostructure in crystals. *Journal of Physics: Condensed Matter* **2007**, *19*, 335219.
(25) Bain, G. A.; Berry, J.F. Diamagnetic Corrections and Pascal's Constants. *J. Chem. Educ.* **2008**, *85*, 532-536.
(26) Krustev, S.; Ivanov, K.; Klissurski, D. Preparation of manganous(II) tungstate by a precipitation method. *J. Alloys Compounds* **1992**, *182*, 189-193.
(27) Farrugia, L.J. Sodium tungstate dihydrate: a redetermination. *Acta Cryst.* **2007**, *E63*, i142.
(28) Yamazoe, S.; Hitomi, Y.; Shishido T.; Tanaka T. XAFS Study of Tungsten L1- and L3-Edges: Structural Analysis of WO_3 Species Loaded on TiO_2 as a Catalyst for Photo-oxidation of NH_3. *J. Phys. Chem. C* **2008**, *112*, 6869-6879.
(29) Farges F. Ab initio and experimental pre-edge investigations of the Mn K-edge XANES in oxide-type materials. *Phys. Rev. B* **2005**, *71*, 155109.
(30) Lautenschläger, G.; Weitzel, H.; Vogt, T.; Hock, R.; Böhm, A.; Bonnet, M.; Fuess, H. Magnetic Phase Transitions of $MnWO_4$ Studied by the Use of Neutron Diffraction. *Phys. Rev. B* **1993**, *48*, 6087–6098.
(31) Ye, F.; Fishman, R. S.; Fernandez-Baca, J. A.; Podlesnyak, A. A.; Ehlers, G.; Mook, H. A.; Wang, Y.; Lorenz, B.; Chu, C. W. Long-range magnetic interactions in the multiferroic antiferromagnet $MnWO_4$. *Phys. Rev. B* **2011**, *83*, 140401.

Table of Contents Synopsis

The structure of ultrasmall nanocrystals of $Mn_{0.8}WO_{3.6}(OH)_4.3H_2O$, which were obtained by a simple salt metathesis reaction involving stoichiometric amounts of manganese(II) chloride and sodium tungstate, was found to be similar to the wolframite structure of bulk-$MnWO_4$.

Table of Contents Graphic